

# THERMAL IMAGING FOR CONTACTLESS CARDIORESPIRATORY AND SUDOMOTOR RESPONSE MONITORING

Constantino Álvarez Casado<sup>\*†</sup>, Mohammad Rahman<sup>\*</sup>, Sasan Sharifipour<sup>\*</sup>,  
Nhi Nguyen<sup>\*</sup>, Manuel Lage Cañellas<sup>\*</sup>, Xiaoting Wu<sup>\*</sup>, Miguel Bordallo López<sup>\*</sup>

<sup>\*</sup>Center for Machine Vision and Signal Analysis (CMVS), University of Oulu, Finland

<sup>†</sup> Research Unit of Health Sciences and Technology (HST), University of Oulu, Oulu, Finland

<sup>†</sup>Candour Ltd, Oulu, Finland

## ABSTRACT

Thermal infrared imaging captures skin temperature changes driven by autonomic regulation and can potentially provide contactless estimation of electrodermal activity (EDA), heart rate (HR), and breathing rate (BR). While visible-light methods address HR and BR, they cannot access EDA, a standard marker of sympathetic activation. This paper characterises the extraction of these three biosignals from facial thermal video using a signal-processing pipeline that tracks anatomical regions, applies spatial aggregation, and separates slow sudomotor trends from faster cardiorespiratory components. For HR, we apply an orthogonal matrix image transformation (OMIT) decomposition across multiple facial regions of interest (ROIs), and for BR we average nasal and cheek signals before spectral peak detection. We evaluate 288 EDA configurations and the HR/BR pipeline on 31 sessions from the public SIMULATOR STUDY 1 (SIM1) driver monitoring dataset. The best fixed EDA configuration (nose region, exponential moving average) reaches a mean absolute correlation of  $0.40 \pm 0.23$  against palm EDA, with individual sessions reaching 0.89. BR estimation achieves a mean absolute error of  $3.1 \pm 1.1$  bpm, while HR estimation yields  $13.8 \pm 7.5$  bpm MAE, limited by the low camera frame rate (7.5 Hz). We report signal polarity alternation across sessions, short thermodynamic latency for well-tracked signals, and condition-dependent and demographic effects on extraction quality. These results provide baseline performance bounds and design guidance for thermal contactless biosignal estimation.

**Index Terms**— Thermal infrared imaging, electrodermal activity, sudomotor response, contactless physiological monitoring, autonomic nervous system, signal processing.

## 1. INTRODUCTION

Contactless monitoring of physiological signals is relevant for remote healthcare, affective computing, and human-machine interaction in safety-critical environments such as industrial

work, training, and driving [1], where skin-contact sensors are impractical or uncomfortable [2]. Most contactless approaches estimate heart rate (HR) and breathing rate (BR) from RGB video or radio-frequency detection [1, 3]. However, estimating electrodermal activity (EDA) from these modalities is less direct, since EDA is defined as changes in skin conductance driven by eccrine sweat gland activity and is conventionally measured with electrodes in contact with the skin [4]. Thermal infrared imaging captures cutaneous temperature fields modulated by perfusion, vasomotor tone, sweating, and convective heat exchange [5, 1]. Figure 1 illustrates how these dynamics can be processed into time series that reflect respiratory oscillations, cardiac-related components, and slower autonomic trends that can be used as EDA-related indicators.

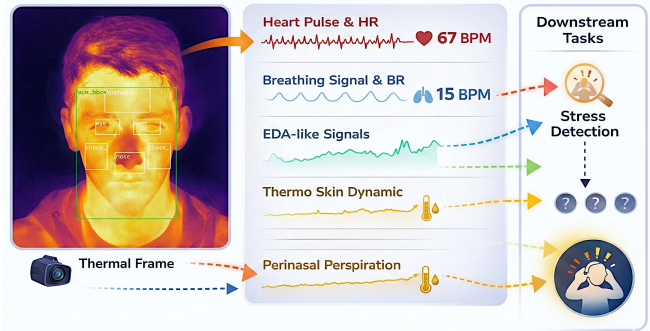


**Fig. 1:** Thermal facial video can be converted into ROI temperature traces and decomposed into respiratory, cardiac-related, and slow autonomic components, including EDA-like trends and perinasal perspiration proxies.

Thermal sensing is independent of visible illumination, but is affected by sensor noise, ambient drift, airflow, and reflections [5]. Together with the limited frame rate of uncooled microbolometers (5–30 Hz) and the thermodynamic latency due to thermal inertia of the tissue, these factors make biosignal extraction challenging. Despite increasing interest, the extent to which HR, BR, and EDA-related dynamics can be recovered from facial thermal video remains insufficiently characterized, and prior work rarely compares multiple facial

regions and extraction choices within a unified evaluation [6].

This paper addresses this gap by characterizing interpretable extraction of EDA-like trends and cardiorespiratory components from facial thermal video. We present a pipeline that detects facial landmarks in thermal frames, defines six anatomical regions of interest (ROIs), extracts ROI temperature traces by spatial aggregation, and applies temporal decomposition to separate slow sudomotor trends, cardiac-related components, and respiratory oscillations. We evaluate the approach on the SIMULATOR STUDY 1 (SIM1) dataset [7], a public corpus with facial thermal sequences and synchronized contact signals, covering 31 sessions from eight subjects under four driving conditions. The analysis compares 288 ROI-method configurations for EDA-like trends and a multi-ROI decomposition strategy for HR and BR, and reports agreement with contact references while examining the influence of condition, sex, and age group.

## 2. RELATED WORK

Thermal cameras capture emitted infrared radiation, typically in the LWIR band ( $7.5\text{--}14\text{ }\mu\text{m}$ ), and convert radiance to apparent temperature through calibration and emissivity assumptions [1, 5]. The human skin emissivity is close to that of a blackbody ( $\varepsilon \approx 0.98$ ), so radiometric measurements approximate the temperature of the superficial skin under controlled conditions. In practice, sensor noise, non-uniformity correction, motion, airflow, and background reflections affect measurement quality [5].

Respiration is the most established target for thermal biosignal extraction, because inhalation and exhalation create temperature oscillations in the perinasal region. The virtual thermistor approach [8] and subsequent extensions have validated the estimation of the breathing rate against contact sensors in laboratory, neonatal and clinical settings [9, 10, 11]. Performance depends on nostril visibility, motion, and thermal contrast [12]. Heart rate estimation from thermal video is less consistent because pulsatile thermal modulation is small and filtered by heat diffusion. Vessel-focused approaches analyse temperature variations along superficial arteries [13, 14], while motion-proxy methods estimate cardiac micro-motion from tracked facial features [15]. Both require stable head pose and typically higher frame rates than standard microbolometers provide. Sudomotor activity is a distinctive opportunity for thermal sensing. Sweat gland activation produces evaporative cooling detectable in high-resolution thermography. Krzywicki et al. [16] detected sweat pore activation correlated with skin conductance responses. Sagaidachnyi et al. [17] proposed spectral separation of sweat-related and haemodynamic components. Gioia et al. [18] applied ICA decomposition to thermal facial video and reported correlations with contact EDA ( $r = 0.9$  median), although under constrained laboratory conditions. Thermal facial patterns have also been used to classify stress, cognitive workload, fatigue, and arousal [6, 19], but these

studies treat temperature as a classification feature rather than reconstructing physiological waveforms.

Across these lines of work, protocols and evaluation metrics differ, and thermodynamic latency from tissue heat transfer is rarely treated explicitly. Most studies focus on a single biosignal and do not compare extraction methods or facial regions in a controlled manner. The present work addresses these gaps by applying a unified pipeline to characterize EDA trend extraction, HR, and BR estimation across multiple ROIs, methods, subjects, and conditions, with lag-tolerant evaluation.

## 3. METHODOLOGY

We propose a four-stage pipeline for the extraction of contactless biosignals from thermal infrared video: anatomical region detection, spatial aggregation, temporal decomposition into three physiological bands, and validation against contact ground truth. Figure 2 shows the workflow.

### 3.1. Detection and ROI Definition

We use YOLOv5-Face [20] with weights from the Thermal Faces in the Wild (TFW) project [21], trained on thermal face data from the SpeakingFaces corpus [22]. Raw 16-bit thermal frames ( $640 \times 512$  pixels) are normalized to 8-bit pseudo-color using a second–98th percentile stretch. The detector outputs a bounding box and five landmarks (left eye, right eye, nose tip, left, and right mouth corners). When multiple faces are detected, the highest-confidence detection is selected. To reduce the jitter of thermal noise, each landmark coordinate  $p_t$  is smoothed with an exponential moving average:  $\hat{p}_t = \alpha p_t + (1 - \alpha) \hat{p}_{t-1}$ , with  $\alpha = 0.15$ .

From the stabilized landmarks, we define six ROIs as axis-aligned rectangles proportional to the face bounding box ( $b_w \times b_h$ ) as shown in Figure 1: nose (centered at the tip of the nose,  $0.30 b_w \times 0.15 b_h$ ), left and right periorbital (near the inner canthus,  $0.24 b_w \times 0.12 b_h$ ), left and right cheek (derived from eye-mouth midpoints with lateral offset,  $0.20 b_w \times 0.20 b_h$ ), and forehead (projected above the inter-eye midpoint,  $0.45 b_w \times 0.18 b_h$ ). All rectangles are clipped to the frame boundaries.

### 3.2. Spatial Aggregation

Given an ROI patch  $\mathbf{P} \in \mathbb{R}^{h \times w}$  of raw thermal values, a spatial aggregation function produces a scalar value per frame. The arithmetic mean is the simplest option, but edge pixels often overlap with background or non-target tissue. We therefore test a Gaussian-weighted mean (2D kernel with  $\sigma = 0.35 \times$  half-width to downweight edges), a trimmed mean (discarding the top and bottom 10% of pixel values), and the mean of the hottest 30% of pixels. We assign Gaussian weighting to the nose, cheeks, and forehead, and trimmed mean to the periorbital regions, based on their noise characteristics.

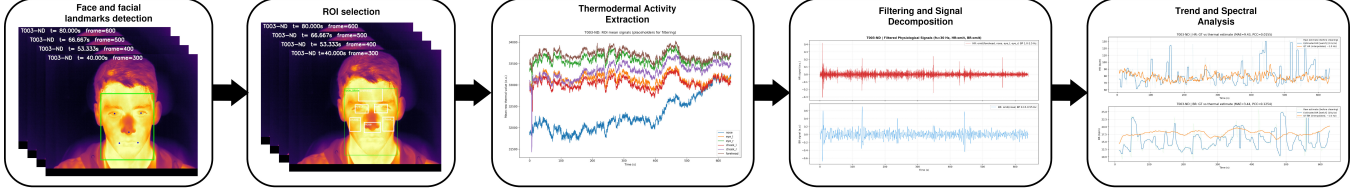


**Fig. 2:** Pipeline overview. Thermal frames are processed by a face detector to localise landmarks. Six facial ROIs are defined and scalar temperature traces are extracted per frame. Temporal decomposition separates slow sudomotor trends, cardiac pulse, and respiratory components for comparison with synchronised contact ground truth.

### 3.3. Temporal Decomposition

ROI signals sampled at native camera rate (7.5 Hz for SIM1) are upsampled to 30 Hz by cubic spline interpolation. The temporal thermal-based signal is then decomposed into three physiological bands.

**Sudomotor trends (EDA-like, <0.1 Hz).** We compare eight extraction methods: Butterworth and Bessel low-pass filters ( $f_c = 0.05$  Hz, 3rd order, zero-phase), Savitzky–Golay filter (30 s window, 3rd order polynomial), simple and exponential moving averages (30 s window), median filter followed by Savitzky–Golay smoothing, Hilbert envelope extraction (bandpass 0.05–3 Hz, amplitude demodulation, then low-pass), and wavelet approximation (Daubechies-4, retaining the low-frequency approximation coefficients). The trends extracted are downsampled to 1 Hz for the calculation of metric.

**Cardiac pulse (1.0–3.5 Hz, 60–210 bpm).** Because pulsatile thermal modulation is weak and spatially distributed, we combine multiple ROIs before spectral analysis. The forehead, nose, and bilateral cheek ROI signals are first pre-filtered with a 4th-order Butterworth bandpass (0.3–4.0 Hz), then combined using an orthogonal matrix image transformation ( OMIT) [3] decomposition. OMIT performs a QR factorization of the multi-channel signal matrix, projects out the dominant (motion-correlated) component, and preserves the residual channel with the highest spectral peak in the cardiac band. The resulting pulse signal is bandpass-filtered (1.0–3.5 Hz, 4th order Butterworth) and passed to a sliding-window Welch spectral estimator (15 s window, 1 s step) with parabolic peak interpolation. Estimated rates outside the valid range (60–180 bpm) are replaced by interpolation over short gaps ( $\leq 10$  samples), followed by a 7-point median filter.

**Respiratory oscillation (0.12–0.55 Hz, 7–33 bpm).** The nose and bilateral cheek signals are pre-filtered (0.12–2.0 Hz bandpass) and averaged to form a combined respiratory signal. The same Welch-based sliding-window estimator is applied (25 s window, 1 s step), with valid-range filtering at 7–45 bpm.

### 3.4. Dataset: SIMULATOR STUDY 1

The SIM1 dataset [7] is a public multimodal corpus acquired during a driving simulator experiment with 68 volunteers. Raw thermal video is stored as 16-bit frames at  $640 \times 512$

pixels,  $\sim 7.5$  fps from a Tau 640 long-wave infrared (LWIR) camera (FLIR Commercial Systems, Goleta, CA). Synchronized contact-based ground truth signals include palm EDA (PEDA, in  $\text{k}\Omega$ ), perinasal perspiration (PP and noise-reduced PP\_NR, in  $^{\circ}\text{C}^2$ ), HR and BR. We select a balanced subset of eight subjects (T002, T003, T005, T014, T029, T031, T034, T036) stratified by sex and age group: four young (two female, two male) and four older (two female, two male). Four driving conditions are analysed per subject: practice drive (PD,  $\sim 3$  min), normal driving (ND), cognitive distraction (CD), and emotional distraction (ED), each  $\sim 10.7$  min. This yields 31 sessions (one excluded due to a missing synchronisation file). Since the pipeline is unsupervised, no training split is needed.

### 3.5. Evaluation Metrics

For EDA, we compute the absolute Pearson correlation  $\text{PCC}_{\text{abs}} = \max(|r(e, r)|, |r(-e, r)|)$  to account for polarity inversions, the Spearman rank correlation  $\rho_s$ , and the maximum normalised cross-correlation  $R_{\text{max}}$  within a  $\pm 120$  s lag window:

$$R_{er}(\tau) = \frac{\sum_i \tilde{e}_{i+\tau} \tilde{r}_i}{\sqrt{\sum_i \tilde{e}_i^2} \sqrt{\sum_i \tilde{r}_i^2}}, \quad (1)$$

where  $\tilde{e}$  and  $\tilde{r}$  are zero-mean unit-variance signals. The lag  $\tau^*$  at maximum  $R_{er}$  estimates the thermodynamic delay. We also compute trend agreement, the percentage of time points where the first differences share the same sign. For HR and BR, we report mean absolute error (MAE), root mean squared error (RMSE), Pearson correlation (PCC), and signed bias, computed on the windowed rate estimates aligned with the contact ground truth.

## 4. EXPERIMENTAL RESULTS

We evaluate 288 EDA configurations (6 ROIs  $\times$  8 methods) and the multi-ROI HR/BR pipeline across 31 sessions.

### 4.1. EDA: Global Agreement

Table 1 reports the best ROI-method combinations. Against PEDa, the nose with exponential MA achieves  $\text{PCC}_{\text{abs}} = 0.40 \pm 0.23$ , followed by the cheeks ( $0.39 \pm 0.24$ ). Against PP\_NR, the cheeks lead ( $0.32 \pm 0.18$ ). If we allow for the selection of the best-configuration per-session (choosing, for

each session, the best ROI and method among the 288 combinations tested), the mean increases to 0.49 (PP\_NR) and 0.54 (PEDA), with peaks of 0.78 and 0.89. Figure 3 shows the full heatmap against PEDDA. Time-domain smoothers outperform frequency-domain alternatives. Compared by methods, the ROI ranking is the following: nose > cheeks  $\approx$  forehead > periorbital. Although the nose achieves the highest mean  $PCC_{abs}$  versus PEDDA in Table 1, the difference to the cheeks is small (0.40 vs 0.39) and both ROIs show a high variability from session-to-session ( $std \approx 0.23$ –0.24). This variability means that ROIs that are slightly weaker on average can still provide better alignment in individual sessions.

**Table 1:** Top EDA ROI-method combinations ( $PCC_{abs}$ , mean  $\pm$  std,  $n = 31$ ).

ROI	Method	vs PP_NR	vs PEDDA
nose	exp. MA	$0.31 \pm 0.18$	<b><math>0.40 \pm 0.23</math></b>
cheeks	exp. MA	<b><math>0.32 \pm 0.18</math></b>	$0.39 \pm 0.24$
nose	mov. avg.	$0.30 \pm 0.20$	$0.38 \pm 0.21$
forehead	exp. MA	$0.31 \pm 0.19$	$0.36 \pm 0.25$
eye_r	exp. MA	$0.28 \pm 0.15$	$0.35 \pm 0.24$
cheeks	mov. avg.	$0.30 \pm 0.18$	$0.34 \pm 0.23$
nose	Bessel LP	$0.29 \pm 0.18$	$0.34 \pm 0.19$
forehead	mov. avg.	$0.27 \pm 0.19$	$0.32 \pm 0.24$

This behavior is visible in qualitative traces. In Figure 4 (T003-CD), the forehead and the eye-average trend follow the broad evolution of the palm sensor more consistently than the nose trace over extended intervals, while the nose signal shows a long deviation that is compatible with local artifacts or polarity-dependent effects. This supports the oracle result reported above: per-session selection improves the mean agreement, and it motivates adaptive ROI selection or multi-ROI fusion rather than relying on a single fixed ROI for all sessions.

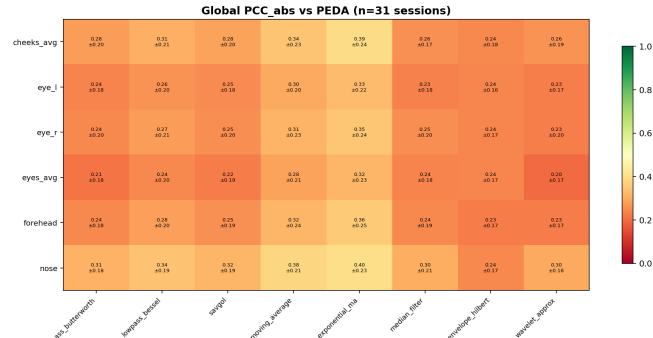


**Fig. 3:**  $PCC_{abs}$  against PEDDA for all 48 ROI-method combinations ( $n = 31$ ).

#### 4.2. HR and BR

The OMIT-based HR pipeline yields  $MAE = 13.8 \pm 7.5$  bpm,  $bias = +10.3$  bpm, and  $PCC \approx 0$ , indicating that at 7.5 Hz the cardiac signal is too weak for reliable tracking. The positive bias suggests the detected spectral peak is often a harmonic or artefact rather than the true cardiac frequency, consistent with

prior reports on low-frame-rate thermal HR estimation [13, 15]. BR estimation is more effective:  $MAE = 3.1 \pm 1.1$  bpm,  $bias = +0.2$  bpm,  $PCC = 0.08 \pm 0.31$ . The practice drive (PD) yields the best BR (MAE = 2.5 bpm, PCC = 0.32), while cognitive distraction (CD) produces the highest error (MAE = 3.7 bpm), likely due to irregular breathing and head movement.

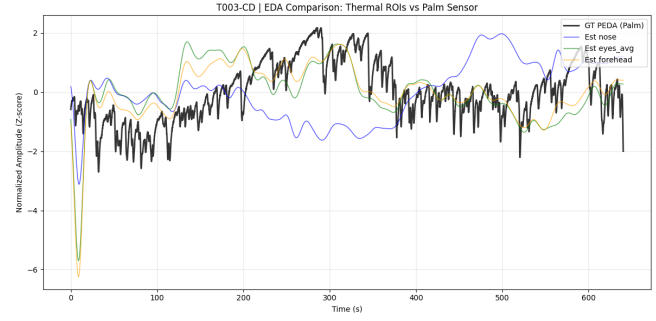


**Fig. 4:** T003-CD: thermal EDA trends from three ROIs vs PEDDA ground truth (black).

#### 4.3. Task, Subject, and Demographic Effects

Figure 5 shows EDA against PEDDA by condition. Normal driving (ND) yields the most stable PP\_NR agreement (cheeks/exp. MA:  $0.42 \pm 0.09$ ). Cognitive distraction shifts the best ROI to the forehead ( $0.38 \pm 0.15$ ), and PD produces the highest PEDDA correlations ( $0.58 \pm 0.21$ ).

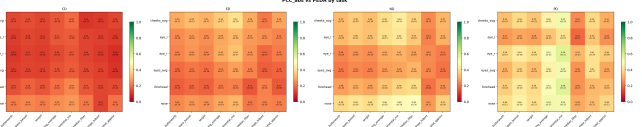


**Fig. 5:**  $PCC_{abs}$  against PEDDA by driving condition ( $n = 7$ –8 per task).

Table 2 reports per-subject EDA. The best  $PCC_{abs}$  ranges from 0.26 to 0.44 (PP\_NR) and 0.35 to 0.67 (PEDDA), with the preferred ROI varying across subjects. Table 3 shows demographic effects. For EDA, both sexes produce similar PEDDA correlations (0.31), while older subjects show slightly higher values (0.32 vs 0.30). For HR, younger subjects achieve lower MAE (8.9 vs 18.3 bpm), suggesting that age-related skin properties may affect cardiac signal quality. BR performance is consistent across groups (MAE  $\approx$  3.0–3.2 bpm). These observations are preliminary given the small sample.

#### 4.4. Latency, Polarity, and Signal Examples

The cross-correlation analysis yields a median lag of 0.0 s for both references, with mean absolute lag  $\approx 19$ –20 s ( $\sigma \approx 32$  s). Of 31 sessions, 55% (PP\_NR) and 77% (PEDDA) peak within  $|\tau| < 30$  s. For well-tracked signals, the latency is typically below 15 s. The thermal-EDA polarity alternates across sessions: 58% positive against PP\_NR, 52% against PEDDA. This near-chance split motivates  $PCC_{abs}$  and indicates that practical systems must handle polarity inversions. The

**Table 2:** Best EDA ROI-method per subject (mean across sessions - n).

Subj.	S/A	n	Best (PP_NR)	Best (PEDA)
T002	F/Y	4	cheeks/eMA $0.44 \pm 0.19$	nose/med $0.36 \pm 0.22$
T003	M/Y	4	nose/mAvg $0.35 \pm 0.23$	cheeks/eMA $0.53 \pm 0.16$
T005	M/Y	3	foreh./med $0.39 \pm 0.09$	cheeks/eMA $0.35 \pm 0.05$
T014	F/Y	4	cheeks/eMA $0.43 \pm 0.19$	cheeks/eMA $0.39 \pm 0.34$
T029	F/O	4	nose/mAvg $0.40 \pm 0.15$	cheeks/eMA <b><math>0.67 \pm 0.21</math></b>
T031	F/O	4	cheeks/eMA $0.26 \pm 0.18$	eye.l/eMA $0.45 \pm 0.23$
T034	M/O	4	nose/mAvg <b><math>0.44 \pm 0.28</math></b>	eye.l/eMA $0.42 \pm 0.25$
T036	M/O	4	nose/eMA $0.38 \pm 0.14$	nose/mAvg $0.43 \pm 0.21$
<i>Mean</i>			$0.39 \pm 0.06$	$0.45 \pm 0.10$

**Table 3:** Demographic effects: EDA (PCC<sub>abs</sub>, Butterworth LP, nose), HR and BR (MAE, bpm).

Group	n	EDA vs PP	EDA vs PEDA	HR MAE	BR MAE
Female	16	$0.22 \pm 0.14$	$0.31 \pm 0.18$	$15.1 \pm 9.7$	$3.0 \pm 2.0$
Male	15	$0.33 \pm 0.19$	$0.31 \pm 0.20$	$12.3 \pm 8.9$	$3.2 \pm 2.1$
Young	15	$0.25 \pm 0.16$	$0.30 \pm 0.23$	$8.9 \pm 8.7$	$3.0 \pm 1.9$
Older	16	$0.28 \pm 0.19$	$0.32 \pm 0.14$	$18.3 \pm 9.9$	$3.2 \pm 2.2$

alternation reflects competing vasoconstriction (cooling) and eccrine sweating (warming) mechanisms. Figure 6 shows session T003-ED. The nose trend (Butterworth LP) tracks the broad PP\_NR shape (PCC = 0.42), while the eyes-average signal (PCC = 0.15) shows less agreement and a tracking artifact near  $t = 250$  s.



**Fig. 6:** T003-ED: PP\_NR and PEDA GT (top), nose ROI vs PP\_NR (middle,  $r = 0.42$ ), eyes ROI (bottom,  $r = 0.15$ ).

## 5. DISCUSSION AND CONCLUSIONS

This study characterizes contactless extraction of sudomotor trends, cardiac pulse, and respiratory rate from facial thermal video. We evaluate 288 EDA configurations across 31 sessions and derive several implications for system design.

For EDA, the nose and cheeks with time-domain smoothers

provide the strongest overall agreement with contact references, reaching mean PCC<sub>abs</sub> = 0.40 against palm EDA and peaks up to 0.89. While the nose is best on average, the differences to cheeks and forehead are small and vary across sessions, indicating that different ROIs capture partially different autonomic components and that session-level ROI selection can be beneficial. Polarity alternates across sessions (approximately 50/50), so practical systems should include polarity detection or polarity-invariant representations. BR estimation achieves MAE of 3.1 bpm with near-zero bias, indicating that respiratory thermal oscillations around the nose and cheeks remain usable at 7.5 Hz. HR estimation yields high MAE (13.8 bpm) and no meaningful temporal correlation, supporting the conclusion that this frame rate is insufficient for reliable thermal cardiac recovery.

Demographic analysis suggests an age effect for HR, with lower MAE for younger subjects (8.9 bpm) than older subjects (18.3 bpm), while BR and EDA are more stable across groups. This may reflect age-related differences in skin and vascular properties, but confirmation requires larger cohorts. Inter-subject variability (best per-subject PCC<sub>abs</sub> from 0.26 to 0.67) and condition-dependent ROI preferences indicate that a fixed pipeline will not generalise well, motivating subject-specific calibration or adaptive multi-ROI fusion. Limitations include the small sample, the low frame rate for HR, and the focus on trend-level rather than event-level EDA evaluation. Future work should test higher-frame-rate cameras, multi-ROI fusion, and validation under broader environmental conditions and larger participant groups.

In general, these results provide baseline performance bounds and identify promising ROIs, filtering choices, and evaluation practices for thermal contactless biosignal extraction, including HR and BR alongside the sudomotor channel.

## 6. REFERENCES

- [1] Zichen Li, Xiaoting Wu, Constantino Álvarez Casado, Ville Lindholm, Kristina Mikkonen, Zhaoqiang Xia, Xiaoyi Feng, and Miguel Bordallo López, “A comprehensive survey on contactless vital sign monitoring using vision-based, radio-based, and fusion approaches,” *Neurocomputing*, vol. 674, pp. 132877, 2026.
- [2] Matan Rubin, Hadar Arnon, Jonathan Huppert, and Anat Perry, “Considering ai-driven therapy: When does human empathy matter? (preprint),” *JMIR Mental Health*, vol. 11, 01 2024.
- [3] Constantino Alvarez Casado and Miguel Bordallo López, “Face2ppg: An unsupervised pipeline for blood volume pulse extraction from faces,” *IEEE Journal of Biomedical and Health Informatics (J-BHI)*, 2022.

[4] Marcin Jukiewicz, Paweł Łupkowski, Radomir Małachowski, Joanna Marcinkowska, and Dawid Ratajczyk, “Electrodermal and thermal measurement of users’ emotional reaction for a visual stimuli,” *Case Studies in Thermal Engineering*, vol. 27, pp. 101303, 2021.

[5] Rikke Gade and Thomas B Moeslund, “Thermal cameras and applications: a survey,” *Machine vision and applications*, vol. 25, no. 1, pp. 245–262, 2014.

[6] Yi Xiao, Harshit Sharma, Zhongyang Zhang, Dessa Bergen-Cico, Tauhidur Rahman, and Asif Salekin, “Reading between the heat: Co-teaching body thermal signatures for non-intrusive stress detection,” *Proceedings of the ACM on Interactive, Mobile, Wearable and Ubiquitous Technologies*, vol. 7, no. 4, pp. 1–30, 2024.

[7] Salah Taamneh, Panagiotis Tsiamyrtzis, Malcolm Dcosta, Pradeep Buddharaju, Ashik Khatri, Michael Manser, Thomas Ferris, Robert Wunderlich, and Ioannis Pavlidis, “A multimodal dataset for various forms of distracted driving,” *Scientific data*, vol. 4, no. 1, pp. 1–21, 2017.

[8] Jianwei Fei and Ioannis Pavlidis, “Thermistor at a distance: Unobtrusive measurement of breathing,” *IEEE Transactions on Biomedical Engineering*, vol. 57, no. 4, pp. 988–998, 2010.

[9] Youngjun Cho, Simon J. Julier, Nicolai Marquardt, and Nadia Bianchi-Berthouze, “Robust tracking of respiratory rate in high-dynamic range scenes using mobile thermal imaging,” *Biomedical Optics Express*, vol. 8, no. 10, pp. 4480–4503, 2017.

[10] Laxmi Maurya, Reyer Zwiggelaar, Deepak Chawla, and Partha Mahapatra, “Non-contact respiratory rate monitoring using thermal and visible imaging: A pilot study on neonates,” *Journal of Clinical Monitoring and Computing*, vol. 37, pp. 815–828, 2023.

[11] Adam Aldred et al., “Application of thermography to estimate respiratory rate in the routine of an emergency room,” *Temperature*, vol. 9, no. 4, pp. 378–386, 2022.

[12] Ilde Lorato, Sander Stuijk, Mohammed Meftah, Deedee Kommers, Peter Andriessen, Carola van Pul, and Gerard de Haan, “Multi-camera infrared thermography for infant respiration monitoring,” *Biomedical Optics Express*, vol. 11, no. 9, pp. 4848–4861, 2020.

[13] Marc Garbey, Nanfei Sun, Arcangelo Merla, and Ioannis Pavlidis, “Contact-free measurement of cardiac pulse based on the analysis of thermal imagery,” *IEEE Transactions on Biomedical Engineering*, vol. 54, no. 8, pp. 1418–1426, 2007.

[14] Sergey Y. Chekmenev, Aly A. Farag, and Edward A. Essock, “Thermal imaging of the superficial temporal artery: An arterial pulse recovery model,” in *Proceedings of the IEEE Conference on Computer Vision and Pattern Recognition Workshops (CVPRW)*, 2007, Best Paper, OTCBVS Workshop.

[15] Carina Barbosa Pereira, Michael Czaplik, Vladimir Blazek, Steffen Leonhardt, and Daniel Teichmann, “Monitoring of cardiorespiratory signals using thermal imaging: A pilot study on healthy human subjects,” *Sensors*, vol. 18, no. 5, pp. 1541, 2018.

[16] Alan T. Krzywicki, Gary G. Berntson, and Barbara L. O’Kane, “A non-contact technique for measuring eccrine sweat gland activity using passive thermal imaging,” *International Journal of Psychophysiology*, vol. 94, no. 1, pp. 25–34, 2014.

[17] Andrey Sagaidachnyi, Dmitriy Mayskov, Andrey Fomin, Ivan Zaletov, and Anatoly Skripal, “Separate extraction of human eccrine sweat gland activity and peripheral hemodynamics from high- and low-quality thermal imaging data,” *Journal of Thermal Biology*, vol. 110, pp. 103351, 2022.

[18] Federica Gioia, Alberto Greco, Alejandro Luis Callara, Nicola Vanello, Enzo Pasquale Scilingo, and Luca Citi, “ThermICA: Novel approach for a multivariate analysis of facial thermal responses,” *IEEE Transactions on Biomedical Engineering*, vol. 72, no. 4, pp. 1237–1247, 2025.

[19] Saurabh Sonkusare, David Ahmedt-Aristizabal, Matthew J. Aburn, Vinh Thai Nguyen, Tianji Pang, Sascha Frydman, Simon Denman, Clinton Fookes, Michael Breakspear, and Christine C. Guo, “Detecting changes in facial temperature induced by a sudden auditory stimulus based on deep learning-assisted face tracking,” *Scientific reports*, vol. 9, no. 1, pp. 4729, 2019.

[20] Delong Qi, Weijun Tan, Qi Yao, and Jingfeng Liu, “YOLO5Face: Why reinventing a face detector,” in *Proceedings of the European Conference on Computer Vision (ECCV) Workshops*. 2022, pp. 228–244, Springer.

[21] Askat Kuzdeuov, Dana Aubakirova, Darina Koishigarina, and Huseyin Atakan Varol, “TFW: Annotated thermal faces in the wild dataset,” *IEEE Transactions on Information Forensics and Security*, vol. 17, pp. 2084–2094, 2022.

[22] Madina Abdurakhmanova, Askat Kuzdeuov, Sheikh Jarju, Yerbolat Khassanov, Michael Lewis, and Huseyin Atakan Varol, “SpeakingFaces: A large-scale multimodal dataset of voice commands with visual and

thermal video streams,” *Sensors*, vol. 21, no. 10, pp. 3465, 2021.